

ARTICLE

Received 26 May 2015 | Accepted 14 Jul 2015 | Published 19 Aug 2015

DOI: 10.1038/ncomms9064

OPEN

Local atomic structure modulations activate metal oxide as electrocatalyst for hydrogen evolution in acidic water

Yu Hang Li¹, Peng Fei Liu¹, Lin Feng Pan¹, Hai Feng Wang², Zhen Zhong Yang³, Li Rong Zheng⁴, P. Hu^{2,5}, Hui Jun Zhao⁶, Lin Gu³ & Hua Gui Yang¹

Modifications of local structure at atomic level could precisely and effectively tune the capacity of materials, enabling enhancement in the catalytic activity. Here we modulate the local atomic structure of a classical but inert transition metal oxide, tungsten trioxide, to be an efficient electrocatalyst for hydrogen evolution in acidic water, which has shown promise as an alternative to platinum. Structural analyses and theoretical calculations together indicate that the origin of the enhanced activity could be attributed to the tailored electronic structure by means of the local atomic structure modulations. We anticipate that suitable structure modulations might be applied on other transition metal oxides to meet the optimal thermodynamic and kinetic requirements, which may pave the way to unlock the potential of other promising candidates as cost-effective electrocatalysts for hydrogen evolution in industry.

¹Key Laboratory for Ultrafine Materials of Ministry of Education, School of Materials Science and Engineering, East China University of Science and Technology, Shanghai 200237, China. ²Key Laboratory for Advanced Materials, Centre for Computational Chemistry and Research Institute of Industrial Catalysis, East China University of Science and Technology, Shanghai 200237, China. ³Institute of Physics, Beijing National Laboratory for Condensed Matter Physics, Chinese Academy of Sciences, Beijing 100190, China. ⁴Beijing Synchrotron Radiation Facility, Institute of High Energy Physics, Chinese Academy of Sciences, Beijing 100049, China. ⁵School of Chemistry and Chemical Engineering, The Queen's University of Belfast, Belfast BT9 5AG, UK. ⁶Centre for Clean Environment and Energy, Gold Coast Campus, Griffith University, Queensland 4222, Australia. Correspondence and requests for materials should be addressed to H.F.W. (email: hfwang@ecust.edu.cn) or to H.G.Y. (email: hgyang@ecust.edu.cn).

Hydrogen, when generated directly from water, would be a promising chemical fuel for sustainable energy applications^{1–5}. Development of hydrogen evolution reaction (HER), $2\text{H}^+ + 2\text{e}^- \rightarrow \text{H}_2$, has attracted worldwide interest^{1,6–8}. Platinum (Pt) can effectively catalyse the electrochemical reduction of protons in acidic media to form molecular hydrogen at low overpotentials⁹, which remains as the most electrocatalytically active catalyst, but its high cost and low abundance limit large-scale commercial application of electrocatalytic hydrogen evolution¹⁰. Thus, efficient Pt-free catalysts are highly desired for facilitating the global scalability of such potential clean energy technology. However, as a large and important class of chemical compounds, most transition metal oxides fail to electrocatalyse hydrogen evolution in acidic water, although numerous carbides, nitrides, phosphides and sulfides have shown the capacity for this reaction^{11–14}.

As an important oxide, tungsten trioxide (WO_3) is much more thermodynamically stable in acidic electrolyte than most metal oxides, and it has attracted intense research interests owing to its potential applications in a wide range of fields such as catalysis, photoelectrochemical cells, photochromic devices and gas sensors^{15–18}. Moreover, recent reports have manifested that WO_3 can act as the support of noble metals and in itself possessing electrocatalytic activity for hydrogen evolution^{19–21}. Unfortunately, the adsorption energy of the atomic hydrogen on W-site is undesirable, leading to the poor activity of WO_3 for HER in acidic media. Noteworthy, as the descriptor of catalytic activity²², the adsorption energies of reactive intermediates can be tuned, in principle, by tailoring the geometric and electronic structures of material, resulting in the enhancement of activity²³. However, modulations of the local structure at the atomic level to tune WO_3 into an active HER catalyst still remains as a great challenge.

Here we present a facile thermal treatment to activate a commercial product of WO_3 into a highly competitive earth abundant catalyst, the dark blue tungsten oxide ($\text{WO}_{2.9}$), for electrocatalysing HER in acidic water (see Fig. 1 for schematic mechanism). Experimentally observed results demonstrate that the $\text{WO}_{2.9}$ with tailored structure exhibits excellent HER activity with a small overpotential of -70 mV at the current density of 10 mA cm^{-2} and a Tafel slope of 50 mV per decade. Further theoretical calculations indicate that its electrocatalytic capacity could be attributed to the modest binding energy with adsorbed

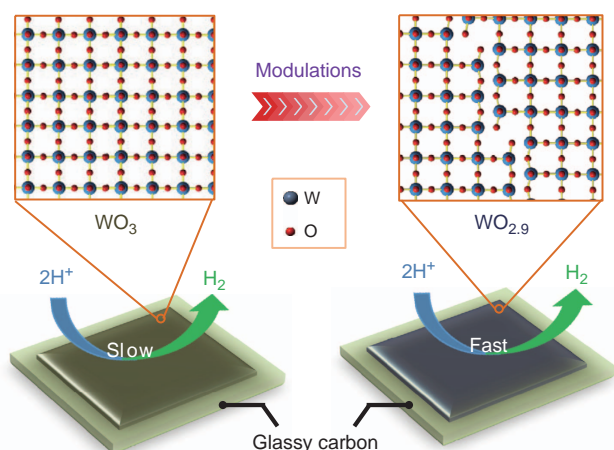


Figure 1 | Plausible reaction mechanism of electrocatalytic H_2 evolution.

By means of local atomic structure modulations, the $\text{WO}_{2.9}$ electrocatalyst with tailored electronic structure exhibits excellent HER activity, whereas the original WO_3 sample is electrocatalytically inactive for proton reduction kinetics.

atomic hydrogen. The findings in this work may hold the promise for the development of more practical non-Pt catalysts for electrocatalytic hydrogen evolution and other scalable technologies that harness renewable energy and convert it to H_2 , for example, the proton exchange membrane electrolysis in acidic environment.

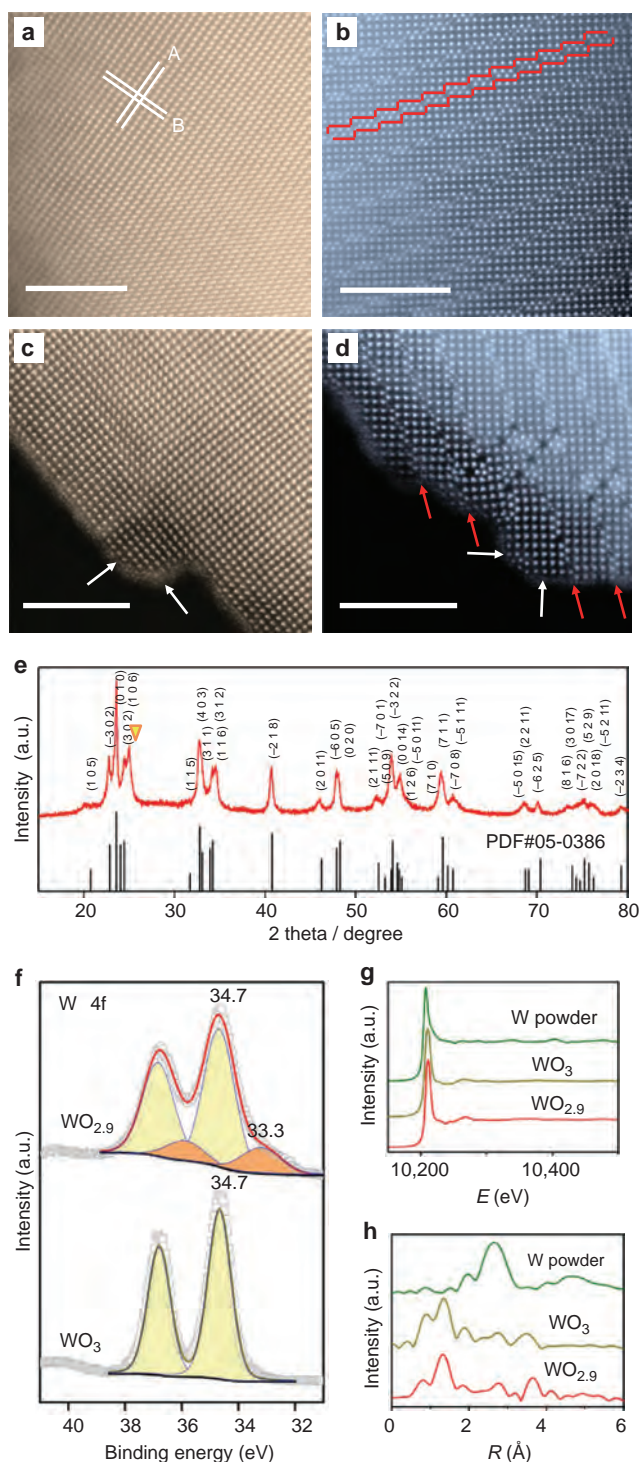
Results

Electron microscopy. To prepare the $\text{WO}_{2.9}$ electrocatalyst, commercially available WO_3 powder was well grinded and thermally treated in a reduction atmosphere, which would readily modulate the local atomic structure of WO_3 (see more details in Methods). The colour of the sample changes from light yellow (commercial product of WO_3) to dark blue after the modifications (Supplementary Fig. 1). Scanning electron microscope (SEM) images reveal the as-prepared $\text{WO}_{2.9}$ nanoparticles with a mean diameter of 100 nm, which exhibits negligible difference comparing to the WO_3 sample (Supplementary Fig. 2), indicating that the modification process in this work may not result in the aggregation of the nanoparticles. Moreover, the energy-dispersive spectrometer mapping, together with corresponding SEM image (Supplementary Fig. 3), clearly shows the existence of the elemental W and O in the $\text{WO}_{2.9}$ sample. To further reveal its structure, a JEM-ARM200F scanning transmission electron microscopy (STEM) fitted with a double aberration corrector for both probe-forming and the imaging lenses is used to perform high-angle annular dark-field (HAADF) imaging. As the contrast exhibits an approximately $Z^{1.7}$ dependency for HAADF imaging, the arrangement of crystallographic structure after modification can be identified directly at the atomic scale. Figure 2 presents the HAADF images of WO_3 and $\text{WO}_{2.9}$ samples, where W atoms are clearly observed (yellow spots for WO_3 and blue spots for $\text{WO}_{2.9}$). As shown in Fig. 2a, WO_3 displays continuous lattice fringes with lattice spacing of 0.382 and 0.366 nm corresponding to the (002) and (200) atomic planes, respectively (white lines, marked as A and B), whereas $\text{WO}_{2.9}$ exhibits an extended and ordered defect structure (Magnéli phase) with a regularly stair-step shape intermittently (red lines in Fig. 2b)²⁴. Specifically, the bulk atomic structure of either WO_3 or $\text{WO}_{2.9}$ sample can also be extended to the surface, indicating the similar geometrical structure between bulk and surface (Fig. 2c,d, marked by white and red arrows). We emphasize that the surfaces and main parts of the local structures between WO_3 and $\text{WO}_{2.9}$ are similar, except for the stair-step shape lattice fringes in $\text{WO}_{2.9}$. This suggests that the tailored electronic structure of the stair-case-shaped lattice fringes would be responsible for the enhanced HER performance of $\text{WO}_{2.9}$.

X-ray analyses. In addition to the HAADF-STEM study, Fig. 2e displays the X-ray diffraction (XRD) pattern of the as-synthesized $\text{WO}_{2.9}$ electrocatalyst. The XRD pattern of the $\text{WO}_{2.9}$ sample contains an extra peak that might belong to the $\text{WO}_{2.83}$ (-404) face (JCPDS Card No. 36-0103), and the other peaks are assigned well to monoclinic $\text{WO}_{2.9}$ bulk (JCPDS Card No. 05-0386). On the other hand, the XRD pattern of WO_3 sample illustrates the pure WO_3 phase (Supplementary Fig. 4, JCPDS No. 43-1035). Besides, the characteristic peaks in Raman spectrum of the sample $\text{WO}_{2.9}$ are broad and weak compared with those of sample WO_3 (see details in Supplementary Fig. 5 and Supplementary Table 1), which could be attributed to the local lattice imperfections²⁵, revealing the absence of partial O atoms in $\text{WO}_{2.9}$ sample. Figure 2f reports our surface analysis for both $\text{WO}_{2.9}$ and WO_3 samples with the X-ray photoelectron spectroscopy (XPS) technique. For the $\text{WO}_{2.9}$ sample, two major tungsten species, W^{6+} ($4f_{7/2} = 34.7$ eV) and W^{5+} ($4f_{7/2} = 33.3$ eV), are found on its surface, showing the existence

of W^{5+} (ref 26). On the other hand, deconvoluted W 4f doublet peaks of the WO_3 sample suggest that tungsten is solely in the state of W^{6+} ($W 4f_{7/2} = 34.7$ eV)²⁷. Moreover, the peaks in the XPS survey scans of the materials before and after the modulations can be only assigned to the W, O and C elements (Supplementary Fig. 6), indicating the inexistence of other elements²⁸. To know the neighbours of the W atoms, the $WO_{2.9}$ sample was thus characterized by means of the W L_3 -edge X-ray absorption fine structure (XAFS). The W L_3 -edge white line derives from electron transitions from the $2p_{3/2}$ state to a vacant $5d$ state, and Fig. 2g presents the W L_3 -edge X-ray absorption near-edge structure spectra of the $WO_{2.9}$ sample and the

reference samples. The Fourier-transformed spectra of W L_3 -edge extended XAFS of the samples are shown in Fig. 2h. The peaks in the range 1–2 Å and around 3 Å appear in the curves of bulk WO_3 and metallic W samples, respectively, owing to the W–O shell and W–W shell. Thus, the only peak in $WO_{2.9}$ sample at 1–2 Å is believed to be the contribution from W–O binding, indicating the absence of metallic W–W bond, which is consistent with the results of XPS W 4f region that the metallic tungsten species (W^0 , $4f_{7/2} = 30.0$ eV) could be hardly detected (Supplementary Fig. 7). On the basis of these results, the tungsten species in the as-synthesized catalyst could be the $WO_{2.9}$ phase with only W–O bond.



Electrochemical hydrogen evolution reaction. The electrodes for HER were prepared by drop casting a fixed volume and concentration of catalysts from an aqueous suspension onto glassy carbon disc (see more details in Methods). The HER with $WO_{2.9}$ nanoparticles as the catalyst on glassy carbon electrode (GCE) was measured using a standard three-electrode electrochemical configuration in 0.5 M H_2SO_4 electrolyte deaerated with hydrogen. The electrodes were prepared by depositing approximately one continuous layer of $WO_{2.9}$ sample over the electrode surface area. The polarization curves (not iR corrected) showing the normalized current density versus voltage (j versus V) for the $WO_{2.9}$ catalyst along with commercial Pt/C (5%) and commercial WO_3 powder for comparison, are shown in Fig. 3a. Compared with blank glassy carbon, the electrode coated with bulk WO_3 exhibits a poor overpotential (η) value of -637 mV at the current density of 10 mA cm^{-2} , demonstrating the electrocatalytically inactive for proton reduction kinetics of the commercial WO_3 powder. In contrast, $WO_{2.9}$ catalyst exhibits a small η value of -70 mV at the current density of 10 mA cm^{-2} , indicating that the tailored structure effectively reduces the energy input for activating the HER. Moreover, for driving a current density of 20 mA cm^{-2} , $WO_{2.9}$ electrocatalyst only requires an overpotential of -94 mV (not iR corrected), indicating a performance evidently exceeding most of the reported noble-metal-free HER catalysts (see details in Supplementary Table 2). These results imply that fast electron transfer and HER activation occur on the $WO_{2.9}$ electrocatalyst (Supplementary Movie 1). Further, the linear portions of the Tafel plots (Fig. 3b) were fit to the Tafel equation ($\eta = b \log j + a$, where j is the current density and b is the Tafel slope)²⁹, yielding Tafel slopes of ~ 30 , ~ 50 and ~ 120 mV per decade for Pt/C, $WO_{2.9}$ and WO_3 samples, respectively. The turnover frequencies (TOFs) were estimated for the η value of -100 and -200 mV using both theoretical and experimental surface areas for the HER in 0.50 M H_2SO_4

Figure 2 | Structure analyses of WO_3 and $WO_{2.9}$ samples. High-angle annular dark-field scanning transmission electron micrograph (HAADF-STEM) images of the samples WO_3 (a,c) and $WO_{2.9}$ (b,d). W atoms can be clearly observed, yellow spots in a,c and blue spots in b,d. The bulk structures for (a) WO_3 , showing continuous lattice fringes (white lines, A for [002] and B for [200]) and (b) $WO_{2.9}$, revealing a regularly stair-step shape (red lines). The typical surface structures for (c) WO_3 and (d) $WO_{2.9}$. White and red arrows point the surface structure that is similar to bulk structure of WO_3 and $WO_{2.9}$, respectively. Scale bar, 5 nm. (e) X-ray diffraction pattern of sample $WO_{2.9}$ we synthesized in this work, which is in good agreement with the calculated diffraction pattern of bulk $WO_{2.9}$ with an extra peak (inverted triangle). theta, diffraction angle. (f) X-ray photoelectron spectroscopy spectra showing the W 4f core level peak region of the samples $WO_{2.9}$ and WO_3 . (g) The normalized X-ray absorption near-edge structure spectra at the W L_3 -edge of the metallic W powder, WO_3 powder and $WO_{2.9}$ catalyst. (h) The k^3 -weighted Fourier transform spectra from extended X-ray absorption fine structure.

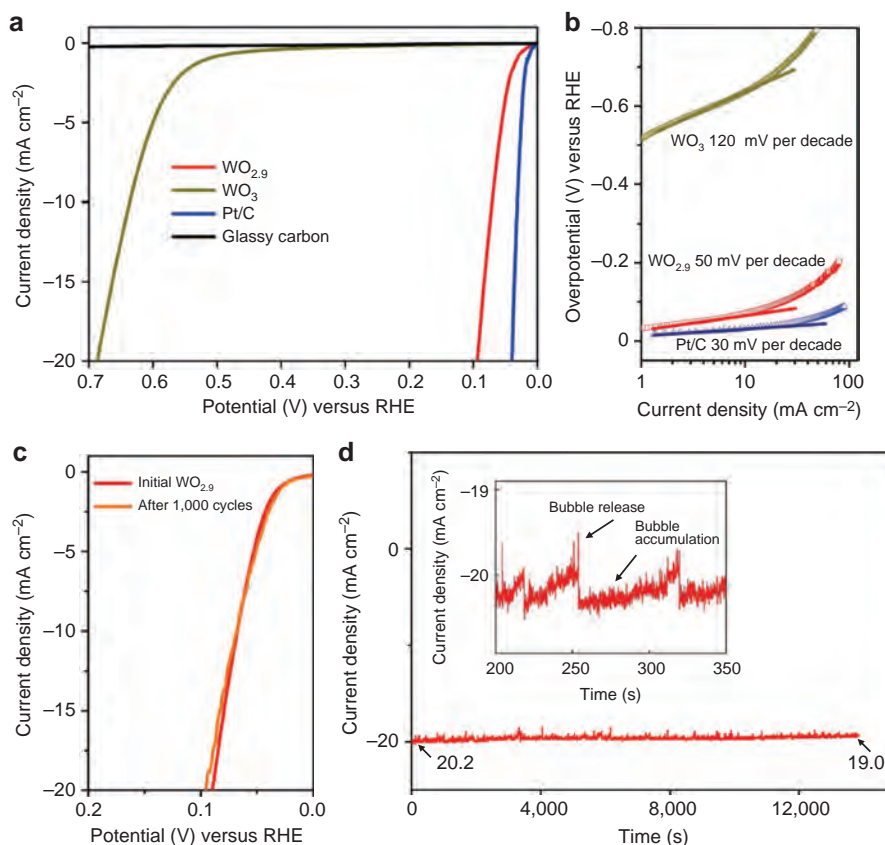


Figure 3 | Hydrogen evolution reaction electrocatalytic properties. (a) Polarization data for the $\text{WO}_{2.9}$ electrodes, along with WO_3 , Pt/C and glassy carbon for comparison. (b) Tafel plots of the polarization curves of the $\text{WO}_{2.9}$, WO_3 and Pt/C. (c) Polarization data for $\text{WO}_{2.9}$ sample sweeps between -0.3 and $+0.1$ V versus RHE, showing negligible current density loss even after 1,000 CV cycles. (d) Time dependence of current density under static overpotential of -0.1 V. Inset is an enlargement of an area in d. All electrochemical studies were performed in 0.5 M H_2SO_4 at room temperature.

Table 1 | Comparison of catalytic parameters of different HER catalysts.

Catalyst	Current density (j , mA cm^{-2})	Corresponding overpotential (η , mV)	Tafel slope (mV per decade)	Exchange current density (j_0 , mA cm^{-2}) ^a
WO_3	10	-637	120	5.0×10^{-5}
$\text{WO}_{2.9}$	10	-70	50	0.40
Pt/C ^b	10	-31	30	0.93

HER, hydrogen evolution reaction; RHE, reversible hydrogen electrode.

^a j_0 was calculated from Tafel curves using extrapolation method.

^bJohnson-Matthey, 20 wt% Pt/XC-72.

(Supplementary Note 1)^{13,30}. The surface area of the $\text{WO}_{2.9}$ catalyst is about $48.3 \text{ m}^2 \text{ g}^{-1}$ determined by Brunauer–Emmett–Teller study, and the TOFs (per surface W atom) were calculated to be 8.04 s^{-1} at -100 mV and 24.76 s^{-1} at -200 mV. Theoretical TOF values, estimated geometrically by assuming 100-nm spherical particles of $\text{WO}_{2.9}$, can be 4.64 s^{-1} at -100 mV and 14.29 s^{-1} at -200 mV. In addition, the HER inherent activity of these catalysts was evaluated by the exchange current density (j_0). The j_0 of $\text{WO}_{2.9}$ catalyst is 0.40 mA cm^{-2} with a surface area of 0.97 cm^2 on the working electrode (0.02 mg loading), which outperforms the value of $5.0 \times 10^{-5} \text{ mA cm}^{-2}$ for bulk WO_3 (Table 1) and can be superior to those for other reported nonprecious HER catalysts (Supplementary Table 2). The high electrode kinetic metrics (including the overpotential of -70 mV at the current density of 10 mA cm^{-2} and the Tafel slope of 50 mV per decade) and large j_0 (only half lower than the

value of 0.93 mA cm^{-2} for Pt) highlight the exceptional H_2 evolving efficiency of the $\text{WO}_{2.9}$ catalyst.

Cyclic voltammetry (CV) was swept between -0.3 and $+0.1$ V (versus the reversible hydrogen electrode potential, RHE) were applied to the $\text{WO}_{2.9}$ -decorated working electrodes (Fig. 3c). After 1,000 CV sweeps, the overpotential required to achieve current densities of 10 mA cm^{-2} shows negligible change (from 70 to 71 mV), which remains higher than those of the benchmark catalysts (Supplementary Table 2). Moreover, we swept the CV towards positive potential up to $+1.0$ V (versus RHE) with scan rate of 0.02 V s^{-1} for 50 times (Supplementary Fig. 8). However, the $\text{WO}_{2.9}$ catalyst shows an undesirable degradation of HER performance, indicating that it could hardly withstand excursions to positive potentials. Continuous HER at a static overpotential was also conducted. As shown in Fig. 3d, when an overpotential of -0.1 V was applied, a continuous HER process occurred to generate molecular H_2 . The as-measured time-dependent curve is in typical serrate shape, which could be attributed to the alternate processes of bubble accumulation and bubble release (inset in Fig. 3d). The amount of the decay of the $\text{WO}_{2.9}$ catalyst is about 5.9% current loss after 14,000 s, which might be owing to the partial detachment of the catalyst caused by the continuous bubbles releasing or the remaining of H_2 bubbles on the surface of the electrode that hindered the reaction. The current density levelled out at an average of 19.6 mA cm^{-2} with the $\text{WO}_{2.9}$ working electrode (0.07 cm^2 surface area, 0.285 mg cm^{-2} loading), resulting in passage of 19.2 C of charge. On the other hand, control experiments run under identical conditions, but with the WO_3 sample and without the catalyst, both showed no current. We further established the HER scale

after the static overpotential test of the $\text{WO}_{2.9}$ catalyst via a gas chromatograph (GC-2014C) with the argon as carrier gas. The total H_2 amount is about $95 \mu\text{mol}$, which is consistent with the theoretical value of $99.5 \mu\text{mol}$ by assuming that every electron is used for the reduction of protons.

In addition, we performed the XRD and XPS techniques to determine the structure of the $\text{WO}_{2.9}$ catalyst after these electrocatalytic tests. As shown in Supplementary Fig. 9, diffraction peaks in pattern of sample $\text{WO}_{2.9}$ remains at the similar intensity and position compared to those in Fig. 2e, revealing the unchanged local structure of $\text{WO}_{2.9}$ catalyst. Moreover, the deconvoluted W 4f doublet peaks of the catalyst after the tests exhibit negligible difference. The dispersion of W^{5+} in both samples, which can be evaluated by the relative XPS intensity ratio of W^{5+} atom to W^{6+} atom, shows negligible change, remaining as 0.182 for the before and after samples. Specifically, we also detected the Pt 4f core level peak region to check for the possible impurities, and the existence of Pt can be thus safely ruled out. All results suggest that the origin of the excellent HER capacity could be attributed to the tailored electronic structure of $\text{WO}_{2.9}$ catalyst by means of local atomic structure modulations.

Density functional theory studies. On the basis of the above experimental investigations, we thus systematically examined the binding ability of their respective most stable surface, that is, $\text{WO}_{2.9}(010)$ and $\text{WO}_3(001)$ by virtue of extensive first-principle density functional theory (DFT) calculations (see details in Fig. 4,

Supplementary Figs 10–13 and Supplementary Note 2). The calculated parameters (Supplementary Table 3) show that the adsorption energy on $\text{WO}_{2.9}(010)$ is largely enhanced relative to that on $\text{WO}_3(001)$. For example, the adsorption energy can be -0.19 eV on $\text{WO}_{2.9}(010)$, and accordingly, the free energy change of the discharge step ($\text{H}^+ + \text{e}^- \rightarrow \text{H}^*$) for HER at the standard condition ($U = 0 \text{ V}$ versus U_{SHE} , $\text{pH} = 0$) can be calculated to be 0.01 eV , fulfilling the $\Delta G_{\text{H}} = 0 \text{ eV}$ requirement, and thus its high catalytic activity could be expected. Moreover, the formed terminal OH could further adsorb H and form H_2O , resulting in the possible reduction. We thus considered the surface reduction by removing all the terminal O from the $p(1 \times 1)$ $\text{WO}_{2.9}(010)$ slab, corresponding to a W/O ratio of $\text{W}_{60}\text{O}_{154}$, whose adsorption energy can be further improved by the order of only $\sim 0.30 \text{ eV}$ compared with the clean $\text{WO}_{2.9}(010)$ surface (Supplementary Table 4). From Fig. 4c, the activity can remain at a high level, despite being a little lower to some extent relative to clean $\text{WO}_{2.9}(010)$. Therefore, it could be rationalized that $\text{WO}_{2.9}$ exhibits a high and stable activity. We further performed a brief electronic analysis to provide insight into the enhanced H adsorption strength of $\text{WO}_{2.9}(010)$. One can see that the highest occupied *d*-orbital of surface W_{5c} largely affects the binding ability toward H atom (Supplementary Figs 14–16), and the appearance of *d*-band around the Fermi level for $\text{WO}_{2.9}(010)$ would be an important factor for the strengthened binding ability compared with WO_3 . In addition, the calculated work function suggests that $\text{WO}_{2.9}$ has a higher Fermi level than WO_3 by 0.70 eV , which may facilitate the reduction process to occur kinetically.

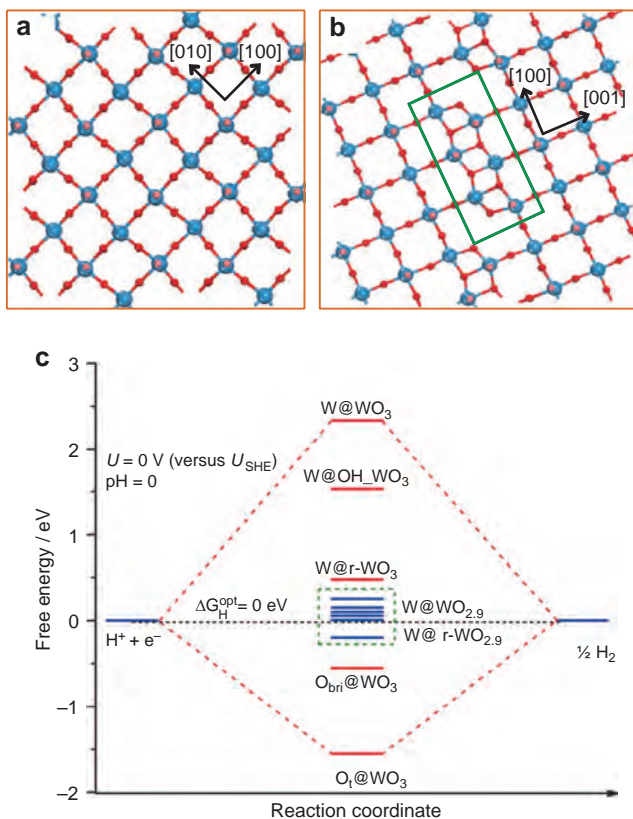


Figure 4 | Density functional theory calculations. Top views of the optimized configuration of monoclinic $\text{WO}_3(001)$ (a) and $\text{WO}_{2.9}(010)$ surface (b), in which the box indicates the new characteristic configuration possessed by $\text{WO}_{2.9}$ relative to WO_3 . Blue balls represent W atom, red for O and pink for the surface terminal O. This notation is used throughout this work. (c) Calculated free energy diagram of HER at the equilibrium potential ($U = U_{\text{SHE}}$) for a series of active sites on $\text{WO}_3(001)$ and $\text{WO}_{2.9}(010)$.

Stability of $\text{WO}_{2.9}$ electrocatalyst. To further probe the stability of the $\text{WO}_{2.9}$ catalyst during electrocatalytic hydrogen evolution in $0.5 \text{ M H}_2\text{SO}_4$, the CV of $\text{WO}_{2.9}$ catalyst was swept between -0.3 and $+0.1 \text{ V}$ for 10,000 times (Supplementary Fig. 17). As with many metal oxides, $\text{WO}_{2.9}$ nanoparticles also suffer from the undesired structure change in acidic water for a long time; they are slightly soluble after these additional accelerated degradation studies, which results in the degradation of electrocatalytic activity. The overpotential increased from -94 to -162 mV at the current density of 20 mA cm^{-2} after 10,000 CV sweeps. XRD pattern in Supplementary Fig. 18 reveals partial formation of $\text{WO}_{2.8}$ phase in catalyst, and the XPS spectrum also shows an enhancement of the W^{5+} doublet peaks in the spectrum from those of fresh $\text{WO}_{2.9}$ sample (Supplementary Fig. 19), indicating the high oxygen vacancies of the atomic structure in acidic water for the rigorous tests. It should be noted, however, that the $\text{WO}_{2.9}$ catalyst is still much more thermodynamically stable in acidic water than most metal oxides. Further investigation is needed to obtain a clear picture of the exact microscopic changes to their surface chemistry and lattice structure. We believe that, with further research, the deactivation may be reduced or eliminated, for example, by integrating $\text{WO}_{2.9}$ nanoparticles with a graphene shell or other nanostructures^{31–33}.

Discussion

The $\text{WO}_{2.9}$ electrocatalyst prepared in this work exhibits excellent HER activity with a very low cathodic overpotential of -70 mV at the current density of 10 mA cm^{-2} and a small Tafel slope of about 50 mV per decade. By modulating the local atomic structure of WO_3 at the atomic scale, an extended and ordered defect structure (Magnéli phase) is formed, resulting in preferentially exposed W sites with modified electronic structure that show a greatly enhanced catalytic activity for hydrogen evolution. We anticipate the transition metal oxide materials with suitable metal hydrogen binding energy may also hold the

promises to compete against the best precious metal catalysts available for HER, compared with the well-studied carbides, nitrides, phosphides and sulfides.

Methods

Synthesis of catalyst. In the preparation of the material, a two-step synthesis process was involved. First, 1 g of commercial WO₃ (of analytically pure grade, 99.9%, Sinopharm) was carefully ground, which was carried out in a ball mill with the wet grinding method (ethanol, 24 h under rotation speed of 300 r.p.m.). Then, we prepared the thermally treated samples through annealing ground WO₃ in hydrogen atmosphere (1 bar, 10% H₂, 90% Ar, 100 s.c.c.m. flow) in a tube furnace at 500 °C for 60 min. The resulting powder can be collected after the tube furnace cooling down to room temperature.

Electrochemical measurements. Four microgram of catalyst and 80 μl of 5 wt% Nafion solution (Sigma-Aldrich) were dispersed in 1 ml of 4:1 v/v water/ethanol by at least 30-min sonication to form a homogeneous ink. Then, 5 μl of the catalyst ink (containing 20 μg of catalyst) was loaded onto a GCE of 3 mm in diameter (loading 0.285 mg cm⁻²). The area of coated electrodes may exceed that of the glassy carbon disc, but we calculate all the current densities using the geometric value. The WO_{2.9} modified GCE was left to dry at 40 °C. For comparison, GCEs were also modified with commercial WO₃ from Sinopharm (99.9%) and Pt/C (5%) from Alfa Aesar.

All electrochemical studies were performed using a CHI 660 potentiostat (CH Instruments, China) in a three-electrode setup with a modified glassy carbon working electrode, an Ag/AgCl/KCl (3.5 M) electrode as a reference, a graphite rod (spectral purity, 3-mm diameter) as a counter electrode and deaerated with hydrogen before use. The electrocatalytic activity of WO_{2.9} towards HER was examined by polarization curves using linear sweep voltammetry at a scan rate of 5 mV s⁻¹ in 0.5 M H₂SO₄ at room temperature. All of the potentials in this work were calibrated to a RHE. The amount of evolved H₂ was monitored by a gas chromatograph (GC-2014C) with argon as carrier gas.

Catalysts characterization. The crystal structure was determined using XRD (D/MAX 2550 VB/PC) and Raman spectroscopy (Renishaw, inVia + Reflex). The structure of the catalysts was examined by SEM (S-3400N) and TEM (TECNAI F-30, 300 kV). Further, the chemical states of the elements in catalysts were studied by XPS (ESCALAB 250Xi), and the binding energy of the C 1s peak at 283.9 eV was taken as an internal reference. W L₃-edge absorption spectra (extended XAFS) were performed on the 1W1B beamline of the Beijing Synchrotron Radiation Facility, China, operated at ~200 mA and ~2.5 GeV. W foil and WO₃ powder were used as the reference samples. All samples were measured in the transmission mode. Brunauer–Emmett–Teller surface area measurement was performed at 77 K on a Micromeritics ASAS 2460 adsorption analyzer in N₂ adsorption mode.

Theoretical calculation. All the spin-polarized calculations were performed with Perdew–Burke–Ernzerhof functional within the generalized gradient approximation using the Vienna Ab-initio Simulation Package (VASP) code, unless otherwise specified. The project-augmented wave method was used to represent the core-valence electron interaction. The valence electronic states were expanded in plane wave basis sets with energy cutoff at 450 eV. The occupancy of the one-electron states was calculated using the Gaussian smearing (SIGMA = 0.05 eV). The ionic degrees of freedom were relaxed using the Broyden–Fletcher–Goldfarb–Shanno (BFGS) minimization scheme until the Hellman–Feynman forces on each ion were <0.05 eV Å⁻¹. The transition states were searched using a constrained optimization scheme, and were verified when (i) all forces on atoms vanish; and (ii) the total energy is a maximum along the reaction coordination but a minimum with respect to the rest of the degrees of freedom.

To model the monoclinic WO₃(001) surface, a nine-layer $c(\sqrt{2} \times \sqrt{2})R45^\circ$ slab (10.772 × 10.805 Å²) with a vacuum layer of 15 Å was adopted, corresponding to (WO₃)₃₂ (128 atoms). For WO_{2.9}(010) surface, an enough large seven-layer $p(1 \times 1)$ slab (23.839 × 12.202 Å²) was used as the model. Because of the large size of the WO_{2.9}(010) supercell, k -point sampling was restricted to the Γ point only. It is worth noting that, all the atomic layers in the optimization of WO_{2.9}(010) were allowed to relax and the surfaces were constructed based on the pre-optimized bulk unit cell (see the optimized lattice constants of the monoclinic WO₃ and WO_{2.9} in Supplementary Table 5).

Free energy calculation method. To obtain the free energy of the each elementary step, when involving H⁺ + e⁻, the standard hydrogen electrode (SHE) was used as the reference in standard Gibbs free energy calculation of HER. As derived in our previous work, Gibbs free energy change (ΔG) of each elementary step can be calculated as follows:

$$\Delta G_1 = E_{\text{ad}}^{\text{H}} + 1/2T\Delta S + eU - kT\ln C_{\text{H}^+} \quad (1)$$

$$\Delta G_2 = -2E_{\text{ad}}^{\text{H}} - T\Delta S + kT\ln P_{\text{H}_2} \quad (2)$$

in which U is the electronic voltage versus SHE, while P_{H_2} and C_{H^+} are the relative partial pressure of H₂ and the relative concentration of H⁺ in the aqueous solution, respectively. At the standard condition, there are approximately $\Delta G_1 = E_{\text{ad}}^{\text{H}} + 0.20$ eV. The adsorption energy (E_{ad}^{H}) for hydrogen was obtained from the DFT calculation at 0 K relative to gas phase H₂ molecule, which is defined as equation (3).

$$E_{\text{ad}}^{\text{H}} = E_{\text{H}/\text{sur}} - E_{\text{sur}} - 1/2E_{\text{H}_2} \quad (3)$$

where $E_{\text{H}/\text{sur}}$ and E_{sur} are the energy of the surface slab with and without atomic H adsorption, and E_{H_2} is the total energy of the H₂ molecule in the gas phase. The more negative E_{ad}^{H} is, the more strongly the species H binds on surface.

References

- Dresselhaus, M. S. & Thomas, I. L. Alternative energy technologies. *Nature* **414**, 332–337 (2001).
- Subbaraman, R. *et al.* Enhancing hydrogen evolution activity in water splitting by tailoring Li⁺-Ni(OH)₂-Pt interfaces. *Science* **334**, 1256–1260 (2011).
- Chen, X., Liu, L., Yu, P. Y. & Mao, S. S. Increasing solar absorption for photocatalysis with black hydrogenated titanium dioxide nanocrystals. *Science* **331**, 746–750 (2011).
- Gao, M.-R. *et al.* An efficient molybdenum disulfide/cobalt diselenide hybrid catalyst for electrochemical hydrogen generation. *Nat. Commun.* **6**, 5982 (2015).
- Zheng, Y. *et al.* Hydrogen evolution by a metal-free electrocatalyst. *Nat. Commun.* **5**, 3783 (2014).
- Evans, D. J. & Pickett, C. J. Chemistry and the hydrogenases. *Chem. Soc. Rev.* **32**, 268–275 (2003).
- Dubois, M. R. & Dubois, D. L. Development of molecular electrocatalysts for CO₂ reduction and H₂ production/oxidation. *Acc. Chem. Res.* **42**, 1974–1982 (2009).
- Inglis, J. L., MacLean, B. J., Pryce, M. T. & Vos, J. G. Electrocatalytic pathways towards sustainable fuel production from water and CO₂. *Coordin. Chem. Rev.* **256**, 2571–2600 (2012).
- Yin, H. *et al.* Ultrathin platinum nanowires grown on single-layered nickel hydroxide with high hydrogen evolution activity. *Nat. Commun.* **6**, 6430 (2015).
- Dempsey, J. L., Brunschwig, B. S., Winkler, J. R. & Gray, H. B. Hydrogen evolution catalyzed by cobaloximes. *Acc. Chem. Res.* **42**, 1995–2004 (2009).
- Chen, W.-F. *et al.* Biomass-derived electrocatalytic composites for hydrogen evolution. *Energy Environ. Sci.* **6**, 1818–1826 (2013).
- Cao, B., Veith, G. M., Neuefeind, J. C., Adzic, R. R. & Khalifah, P. G. Mixed close-packed cobalt molybdenum nitrides as non-noble metal electrocatalysts for the hydrogen evolution reaction. *J. Am. Chem. Soc.* **135**, 19186–19192 (2013).
- Popczun, E. J. *et al.* Nanostructured nickel phosphide as an electrocatalyst for the hydrogen evolution reaction. *J. Am. Chem. Soc.* **135**, 9267–9270 (2013).
- Kibsgaard, J., Chen, Z., Reinecke, B. N. & Jaramillo, T. F. Engineering the surface structure of MoS₂ to preferentially expose active edge sites for electrocatalysis. *Nat. Mater.* **11**, 963–969 (2012).
- Liu, Y., Luo, C. & Liu, H. Tungsten trioxide promoted selective conversion of cellulose into propylene glycol and ethylene glycol on a ruthenium catalyst. *Angew. Chem. Int. Ed. Engl.* **51**, 3249–3253 (2012).
- Shi, X. *et al.* Efficient photoelectrochemical hydrogen production from bismuth vanadate-decorated tungsten trioxide helix nanostructures. *Nat. Commun.* **5**, 4775 (2014).
- Lorenz, M., Wenckstern, H. & Grundmann, M. Tungsten oxide as a gate dielectric for highly transparent and temperature-stable zinc-oxide-based thin-film transistors. *Adv. Mater.* **23**, 5383–5386 (2011).
- Devan, R. S., Patil, R. A., Lin, J.-H. & Ma, Y.-R. One-dimensional metal-oxide nanostructures: recent developments in synthesis, characterization, and applications. *Adv. Funct. Mater.* **22**, 3326–3370 (2012).
- Maiyalagan, T. & Viswanathan, B. Catalytic activity of platinum/tungsten oxide nanorod electrodes towards electro-oxidation of methanol. *J. Power Sources* **175**, 789–793 (2008).
- Wickman, B., Wesselmark, M., Lagergren, C. & Lindbergh, G. Tungsten oxide in polymer electrolyte fuel cell electrodes—a thin-film model electrode study. *Electrochim. Acta* **56**, 9496–9503 (2011).
- Ganesan, R. & Gedanken, A. Synthesis of WO₃ nanoparticles using a biopolymer as a template for electrocatalytic hydrogen evolution. *Nanotechnology* **19**, 025702 (2008).
- Greeley, J., Jaramillo, T. F., Bonde, J., Chorkendorff, I. & Nørskov, J. K. Computational high-throughput screening of electrocatalytic materials for hydrogen evolution. *Nat. Mater.* **5**, 909–913 (2006).
- Chen, C. *et al.* Highly crystalline multimetallic nanoframes with three-dimensional electrocatalytic surfaces. *Science* **343**, 1339–1343 (2014).
- Kieslich, G. *et al.* Enhanced thermoelectric properties of the n-type Magnéli phase WO_{2.90}: reduced thermal conductivity through microstructure engineering. *J. Mater. Chem. A* **2**, 13492–13497 (2014).

25. Zhang, W. F., He, Y. L., Zhang, M. S., Yin, Z. & Chen, Q. Raman scattering study on anatase TiO₂ nanocrystals. *J. Phys. D: Appl. Phys.* **33**, 912–916 (2000).
26. Wang, G. *et al.* Hydrogen-treated WO₃ nanoflakes show enhanced photostability. *Energy Environ. Sci.* **5**, 6180–6187 (2012).
27. Xie, F. Y. *et al.* XPS studies on surface reduction of tungsten oxide nanowire film by Ar⁺ bombardment. *J. Electron. Spectrosc. Relat. Phenom.* **185**, 112–118 (2012).
28. Zhuiykov, S., Kats, E., Carey, B. & Balendhran, S. Proton intercalated two-dimensional WO₃ nano-flakes with enhanced charge-carrier mobility at room temperature. *Nanoscale* **6**, 15029–15036 (2014).
29. Vrabel, H. & Hu, X. Molybdenum boride and carbide catalyze hydrogen evolution in both acidic and basic solutions. *Angew. Chem. Int. Ed. Engl.* **51**, 12703–12706 (2012).
30. Song, F. & Hu, X. Ultrathin cobalt–manganese layered double hydroxide is an efficient oxygen evolution catalyst. *J. Am. Chem. Soc.* **136**, 16481–16484 (2014).
31. Xu, Y.-F., Gao, M.-R., Zheng, Y.-R., Jiang, J. & Yu, S.-H. Nickel/nickel(II) oxide nanoparticles anchored onto cobalt(IV) diselenide nanobelts for the electrochemical production of hydrogen. *Angew. Chem. Int. Ed. Engl.* **52**, 8546–8550 (2013).
32. Deng, J. *et al.* Highly active and durable non-precious-metal catalysts encapsulated in carbon nanotubes for hydrogen evolution reaction. *Energy Environ. Sci.* **7**, 1919–1923 (2014).
33. Deng, J., Ren, P., Deng, D. & Bao, X. Enhanced electron penetration through an ultrathin graphene layer for highly efficient catalysis of the hydrogen evolution reaction. *Angew. Chem. Int. Ed. Engl.* **54**, 2100–2104 (2015).

Acknowledgements

This work was financially supported by the Science Fund for Creative Research Groups (21421004), National Natural Science Foundation of China (21373083 and 21303052), SRF for ROCS, SEM, SRFDP, Programme for Professor of Special Appointment (Eastern Scholar) at Shanghai Institutions of Higher Learning, Program of Shanghai Subject Chief Scientist (15XD1501300), and Fundamental Research Funds for the Central Universities

(WD1313009, 222201314035), the Commission of Science and Technology of Shanghai Municipality (12ZR1442600).

Author contributions

H.G.Y. conceived the project and contributed to the design of the experiments and analysis of the data. Y.H.L. performed the catalyst preparation, characterizations and wrote the paper. Z.Z.Y. and L.G. conducted the STEM examination and contributed to writing the STEM section. L.F.P., P.F.L. and H.J.Z. collected the electrochemical data. L.R.Z. carried out measurements and data analyses of XAFS. H.F.W. and P.H. conducted DFT calculations and wrote part of the paper (calculations). All the authors discussed the results and commented on the manuscript.

Additional information

Supplementary Information accompanies this paper at <http://www.nature.com/naturecommunications>

Competing financial interests: The authors declare no competing financial interests.

Reprints and permission information is available online at <http://npg.nature.com/reprintsandpermissions/>

How to cite this article: Li, Y. H. *et al.* Local atomic structure modulations activate metal oxide as electrocatalyst for hydrogen evolution in acidic water. *Nat. Commun.* **6**:8064 doi: 10.1038/ncomms9064 (2015).



This work is licensed under a Creative Commons Attribution 4.0 International License. The images or other third party material in this article are included in the article's Creative Commons license, unless indicated otherwise in the credit line; if the material is not included under the Creative Commons license, users will need to obtain permission from the license holder to reproduce the material. To view a copy of this license, visit <http://creativecommons.org/licenses/by/4.0/>